Acta Geotechnica (2006) 1:211–224
DOI 10.1007/s11440-006-0017-5

RESEARCH PAPER

# Condition for liquefaction instability in fluid-saturated granular soils

**Ronaldo I. Borja**

Received: 1 September 2006 / Accepted: 10 October 2006 / Published online: 24 November 2006


**Abstract** High-porosity granular materials such as loose sands can implode when subjected to compressive stresses. The mechanism of deformation is diffuse in that the jump in the strain rate tensor has three independent eigenvalues (full rank), in contrast to the jump in the strain rate tensor for a deformation band-type instability that has one eigenvalue (rank one). Recently, the mechanism of volume implosion has been studied in the context of material instability. In this paper we move one step further and consider the effect of a volume constraint associated with the presence of fluids in the pores of granular materials that have a tendency to implode. The upshot of this constraint is that at the onset of liquefaction the solid matrix deforms in a nearly isochoric fashion at the same time that the pore fluid pressure increases. The corresponding eigenmode (e-mode) is represented by jumps in the strain rate tensor and rate of pore fluid pressure. The framework presented in this work is used to analyze the onset of liquefaction instability in very loose Hostun RF sand tested in undrained triaxial compression and extension.

**Keywords** Bifurcation · Instability · Liquefaction · Undrained condition · Saturated sands

## 1 Introduction

Liquefaction occurs when a saturated granular soil is converted into a liquid. Soil liquefaction can damage structures in many ways as the supporting ground sinks or even pulls apart [19, 21, 23]. The physical mechanism of liquefaction is well understood. If we subject an assembly of loose, dry sands either to static or dynamic loading, the grain-to-grain contacts will eventually collapse until the particles find a more stable, denser configuration. The process is not that of stable compaction or densification since the volume changes abruptly, suggesting momentary loss of stability, and so the term 'volume implosion' seems more apt to characterize the process. However, if the same loose sand is fully saturated and subjected to the same load, implosion is not possible since the water is trapped in the pores and cannot compress. As the water is squeezed inside the collapsing pores, the fluid pressure rapidly increases causing the contact forces between the particles to disappear. Thus the soil is converted into a suspension. For many years now a persistent question has been that of finding the trigger for liquefaction. What mathematical condition signals the onset of liquefaction instability?

Soil liquefaction is a multiscale, multiphysics problem, originating at the pore scale level but rapidly propagating to the particle cluster and specimen scales. Particulate mechanics can shed much light onto what transpires at the particle scale [15, 17, 39] leading to 'instability' at the macroscale, including particle motion and the associated pore-scale hydrodynamics. However, because slip at a particle contact does not necessarily constitute what we would normally consider as collapse at the macroscale, it is difficult to infer when liquefaction has occurred from the motion of the individual particles alone. The process needs to be propagated to the macroscale level to have a more meaningful definition of 'liquefaction.' Hence, whereas

R. I. Borja (✉)
Department of Civil and Environmental Engineering,
Stanford University, Stanford, CA 94305, USA
e-mail: borja@stanford.edu

particulate mechanics provides insight into the more fundamental mechanism of pore collapse, we shall take a macroscale approach in our characterization of the trigger for liquefaction.

Two macroscale criteria for failure in soils are commonly employed for interpreting triaxial test results [24, 38]: (a) when the principal stress difference reaches a maximum value, $(\sigma_1-\sigma_3)_{\max}$; and (b) when the effective principal stress ratio reaches a peak value, $(\sigma'_1/\sigma'_3)_{\max}$. The two conditions are reached simultaneously in drained tests, but not in undrained tests where confusion arises as to what constitutes 'instability' and what constitutes 'failure.' This is most unfortunate considering that liquefaction occurs during undrained testing, and not during drained testing. Similar macroscale criteria but based on the use of a so-called flow liquefaction surface along with a steady-state line have been developed for undrained triaxial testing on loose sands [31, 35–37].

The macroscale criteria stated above are based solely on triaxial stress paths and do not extend directly to three-dimensional loading conditions. Also, they do not reflect the kinematics of deformation at the moment of instability, whether the sample failed by liquefaction or by deformation banding. Finally, the procedure assumes that the sample is deforming homogeneously throughout testing that it suffices to determine the stresses from the total loads applied to the sample. Recently, it has been demonstrated that minute perturbations in the density of the soil sample could trigger deformation banding [2, 8]. A heterogeneous sample sheared at a given mean density could be simulated to localize into a shear band, even if the imposed heterogeneity is very slight, when the equivalent homogeneous sample with the same density would not manifest any form of instability. It may be argued that this could also be true with liquefaction instability simulations.

Our point of departure in this paper is the definition of incremental stability revisited and elaborated by Borja [6] for the case of single phase solid materials. Loss of stability occurs when the constitutive tangent operator becomes singular and results in non-unique strain rates. The condition coincides with that of a stationary stress rate (for a symmetric constitutive tangent operator), and the calculated eigen-strain rates define the corresponding eigenmode (e-mode). In general the e-mode has a full determinant rank, three for a 3D problem, for example, and can be fully quantified, including its sign, except for its norm. Now, if the e-mode is assumed to have the form of a slip tensor of determinant rank one, then loss of stability coincides with the loss of ellipticity of the governing problem (for a symmetric acoustic tensor). In physical terms the e-mode defines a deformation band and is determined from the condition of stationary traction rates [33]. Evidently, a full-rank e-mode is more appropriate for investigating the onset of liquefaction instability. We shall describe such e-mode as "diffuse," as opposed to the rank-one e-mode which we shall term "localized."

For a mixture consisting of solids and fluids it is not so evident what constitutive tangent operator must become singular to signal the onset of liquefaction. We thus resort to an integral expression first used by Hill [18] to demonstrate a general theory of uniqueness and stability in elastoplastic solids. We show that for undrained bifurcation the relevant constitutive tensor pertains to that of the total mixture, even if the solid skeleton follows a constitutive law that utilizes the effective stresses. The presence of pore fluids imposes a volume constraint that alters the e-mode; this constraint is derived from balance of mass which we develop in this paper in a form that accommodates for the compressibility of both the solid grains and fluids. Finally, we demonstrate with a numerical example the triggering of liquefaction instability in a loose, saturated sand. The e-mode, often neglected in many stability analyses, is in fact very crucial in describing the associated kinematic bifurcation response since it indicates whether the type of instability is diffuse or localized. Thus, we also calculate the e-mode consistent with the identified singular point. Since liquefaction often entails large deformation, we shall adopt nonlinear continuum mechanics throughout this paper.

As for notations and symbols, bold-faced letters denote tensors and vectors; the symbol '$\cdot$' denotes an inner product of two vectors (e.g. $\boldsymbol{a}\cdot\boldsymbol{b}=a_ib_i$), or a single contraction of adjacent indices of two tensors (e.g. $\boldsymbol{c}\cdot\boldsymbol{d}=c_{ij}d_{jk}$); the symbol ':' denotes an inner product of two second-order tensors (e.g. $\boldsymbol{c}:\boldsymbol{d}=c_{ij}d_{ij}$), or a double contraction of adjacent indices of tensors of ranks two and higher (e.g. $\boldsymbol{C}:\boldsymbol{\epsilon}=C_{ijkl}\epsilon_{kl}$); the symbol '$\otimes$' denotes a juxtaposition of two vectors, $(\boldsymbol{a}\otimes\boldsymbol{b})_{ij}=a_ib_j$, or of two symmetric second-order tensors, $(\boldsymbol{\alpha}\otimes\boldsymbol{\beta})_{ijkl}=\alpha_{ij}\beta_{kl}$.

## 2 Balance laws

### 2.1 Balance of mass

Consider a two-phase mixture composed of a solid matrix whose voids are continuous and completely filled with fluid (see [4, 5, 7, 26] for a detailed mathematical background). We denote the volume fraction by $\phi^\alpha=V_\alpha/V$ for $\alpha=$ solid and fluid, where $V_\alpha$ is the

portion of the total volume $V$ of the mixture occupied by constituent $\alpha$. The volume fractions satisfy the saturation condition

$$\phi^{\mathrm{s}} + \phi^{\mathrm{f}} = 1. \tag{1}$$

The partial mass density is $\rho^{\alpha} = \phi^{\alpha}\rho_{\alpha}$, where $\rho_{\alpha}$ is the intrinsic mass density, so the total mass density of the mixture is

$$\rho = \rho^{\mathrm{s}} + \rho^{\mathrm{f}}. \tag{2}$$

We denote the time derivative with respect to the solid motion by

$$\frac{\mathrm{d}(\cdot)}{\mathrm{d}t} = \frac{\partial(\cdot)}{\partial t} + \mathrm{grad}(\cdot)\cdot\boldsymbol{v}, \tag{3}$$

where $\boldsymbol{v}$ is the velocity of the solid and grad is the spatial gradient operator. In this paper we shall take the more abbreviated superposed dot to mean the same time derivative, i.e. $\dot{a} = \mathrm{d}a/\mathrm{d}t$. The time derivative with respect to the fluid motion is given by

$$\frac{\mathrm{d}^{\mathrm{f}}(\cdot)}{\mathrm{d}t} = \frac{\partial(\cdot)}{\partial t} + \mathrm{grad}(\cdot)\cdot\boldsymbol{v}_{\mathrm{f}}, \tag{4}$$

where $\boldsymbol{v}_{\mathrm{f}}$ is the velocity of the fluid. The two time derivatives in (3) and (4) are related by the equation

$$\frac{\mathrm{d}^{\mathrm{f}}(\cdot)}{\mathrm{d}t} = \frac{\mathrm{d}(\cdot)}{\mathrm{d}t} + \mathrm{grad}(\cdot)\cdot\widetilde{\boldsymbol{v}}, \quad \widetilde{\boldsymbol{v}} = \boldsymbol{v}_{\mathrm{f}} - \boldsymbol{v}. \tag{5}$$

In terms of the motion of the solid, balance of mass for the solid and fluid are given, respectively, by

$$\frac{\mathrm{d}\rho^{\mathrm{s}}}{\mathrm{d}t} + \rho^{\mathrm{s}}\mathrm{div}(\boldsymbol{v}) = 0, \tag{6}$$

$$\frac{\mathrm{d}\rho^{\mathrm{f}}}{\mathrm{d}t} + \rho^{\mathrm{f}}\mathrm{div}(\boldsymbol{v}) = -\mathrm{div}(\boldsymbol{q}), \tag{7}$$

where $\boldsymbol{q} = \rho^{\mathrm{f}}\widetilde{\boldsymbol{v}}$ is the Eulerian relative flow vector of the fluid relative to the solid, $\widetilde{\boldsymbol{v}} = \boldsymbol{v}_{\mathrm{f}} - \boldsymbol{v}$ is the relative velocity of the fluid to the solid, and div is the spatial divergence operator.

For barotropic flows [27] the intrinsic bulk modulus of the constituent $\alpha$ can be defined as

$$K_{\alpha} = \rho_{\alpha}p'_{\alpha}(\rho_{\alpha}), \tag{8}$$

where $p_{\alpha}$ is the intrinsic Cauchy pressure in the $\alpha$ constituent (compressive normal force acting on this constituent per unit area of the same constituent). Here we assume that $p_{\alpha}$ has a functional relationship with the intrinsic mass density $\rho_{\alpha}$. The bulk modulus $K_{\alpha}$ is a property of the material, and in this paper we shall assume this quantity to be constant for the solid and fluid. Essentially this implies that for barotropic flow the functional relation takes the logarithmic form

$$p_{\alpha} = p_{\alpha 0} + K_{\alpha}\ln\left(\frac{\rho_{\alpha}}{\rho_{\alpha 0}}\right), \tag{9}$$

where $p_{\alpha 0}$ is the intrinsic pressure at reference intrinsic mass density $\rho_{\alpha 0}$. Inserting (8) into (6) and (7) gives

$$\frac{\mathrm{d}\phi^{\mathrm{s}}}{\mathrm{d}t} + \frac{\phi^{\mathrm{s}}}{K_{\mathrm{s}}}\frac{\mathrm{d}p_{\mathrm{s}}}{\mathrm{d}t} + \phi^{\mathrm{s}}\mathrm{div}(\boldsymbol{v}) = 0, \tag{10}$$

$$\frac{\mathrm{d}\phi^{\mathrm{f}}}{\mathrm{d}t} + \frac{\phi^{\mathrm{f}}}{K_{\mathrm{f}}}\frac{\mathrm{d}p_{\mathrm{f}}}{\mathrm{d}t} + \phi^{\mathrm{f}}\mathrm{div}(\boldsymbol{v}) = -\frac{1}{\rho_{\mathrm{f}}}\mathrm{div}(\boldsymbol{q}). \tag{11}$$

Next we set

$$\phi^{\mathrm{s}}\frac{\mathrm{d}p_{\mathrm{s}}}{\mathrm{d}t} = -K\mathrm{div}(\boldsymbol{v}), \tag{12}$$

where $K$ is the bulk modulus of the solid matrix (not to be confused with the intrinsic bulk modulus $K_{\mathrm{s}}$ for the solid constituent). A specific form for $K$ may be derived from an assumed functional relationship among the state variables $p_{\mathrm{s}}$, $\rho_{\mathrm{s}}$ and $\phi^{\mathrm{s}}$ [7]. Adding (10) and (11) and inserting (12) results in the following balance of mass for the mixture in Eulerian form

$$B\mathrm{div}(\boldsymbol{v}) + \frac{\phi^{\mathrm{f}}}{K_{\mathrm{f}}}\frac{\mathrm{d}p_{\mathrm{f}}}{\mathrm{d}t} = -\frac{1}{\rho_{\mathrm{f}}}\mathrm{div}(\boldsymbol{q}), \tag{13}$$

where

$$B := 1 - \frac{K}{K_{\mathrm{s}}} \tag{14}$$

is the Biot coefficient. For soils $K \ll K_{\mathrm{s}}$, and $B$ may be assumed equal to unity.

Now, let $\boldsymbol{F}$ denote the deformation gradient of the solid motion and $J = \det(\boldsymbol{F})$ represent the corresponding Jacobian. We define the Kirchhoff pore fluid pressure as

$$\theta_{\mathrm{f}} = Jp_{\mathrm{f}}, \tag{15}$$

with material time derivative, relative to the solid motion, given by

$$\frac{\mathrm{d}\theta_{\mathrm{f}}}{\mathrm{d}t} = J\frac{\mathrm{d}p_{\mathrm{f}}}{\mathrm{d}t} + p_{\mathrm{f}}\frac{\mathrm{d}J}{\mathrm{d}t}, \tag{16}$$

in which $\mathrm{d}J/\mathrm{d}t \equiv \dot{J} = J\mathrm{div}(\boldsymbol{v})$ following nonlinear continuum mechanics. The Lagrangian form of (13) may then be written by introducing $J$ on both sides of this equation and using the Piola identity to get

$$\left(B-\frac{p^{\mathrm{f}}}{K_{\mathrm{f}}}\right)\frac{\mathrm{d}J}{\mathrm{d}t}+\frac{\phi^{\mathrm{f}}}{K_{\mathrm{f}}}\frac{\mathrm{d}\theta_{\mathrm{f}}}{\mathrm{d}t}=-\frac{1}{\rho_{\mathrm{f}}}\mathrm{DIV}(\boldsymbol{Q}), \tag{17}$$

where $p^{\mathrm{f}} = \phi^{\mathrm{f}} p_{\mathrm{f}}$ is the partial pore fluid pressure,

$$\boldsymbol{Q}=J\boldsymbol{F}^{-1}\cdot\boldsymbol{q} \tag{18}$$

is the Piola transform of $\boldsymbol{q}$, and DIV is the divergence operator evaluated with respect to the reference configuration. We shall provide a physical meaning to the Piola transform $\boldsymbol{Q}$ in the next section.

We now consider a solid body with initial placement $\mathcal{B}$ and bounded by surface $\partial\mathcal{B}$, where the latter admits the decomposition $\partial\mathcal{B}=\overline{\partial\mathcal{B}_\theta\cup\partial\mathcal{B}_q}$ and $\emptyset=\partial\mathcal{B}_\theta\cap\partial\mathcal{B}_q$; and where $\partial\mathcal{B}_\theta$ and $\partial\mathcal{B}_q$ are portions of the entire boundary where the Kirchhoff fluid pressures and velocity fluxes are prescribed. Balance of mass for the mixture takes the form

$$\left(B-\frac{p^{\mathrm{f}}}{K_{\mathrm{f}}}\right)\dot{J}+\frac{\phi^{\mathrm{f}}}{K_{\mathrm{f}}}\dot{\theta}_{\mathrm{f}}=-\frac{1}{\rho_{\mathrm{f}}}\mathrm{DIV}(\boldsymbol{Q}) \qquad \text{in } \mathcal{B} \tag{19}$$

$$\dot{\theta}_{\mathrm{f}}=\dot{\theta}_{\mathrm{f0}} \qquad \text{on } \partial\mathcal{B}_\theta \tag{20}$$

$$\boldsymbol{Q}\cdot\boldsymbol{N}=Q_0 \qquad \text{on } \partial\mathcal{B}_q \tag{21}$$

We note that $\boldsymbol{Q}\cdot\boldsymbol{N}=\boldsymbol{q}\cdot\boldsymbol{n}$, where $\boldsymbol{n}=J\boldsymbol{N}\cdot\boldsymbol{F}^{-1}$ is the push-forward of the reference unit normal $\boldsymbol{N}$ (cf. Nanson's formula, see [30]).

## 2.2 Balance of linear momentum

Without loss of generality we shall consider a quasi-static loading condition and write the balance of linear momentum in Lagrangian form as

$$\mathrm{DIV}(\boldsymbol{P})+\rho_0\mathbf{g}=\mathbf{0}, \qquad \rho_0=J\rho, \tag{22}$$

where $\boldsymbol{P}$ is the first Piola–Kirchhoff total stress tensor, $\mathbf{g}$ is the gravity acceleration vector, and $\rho$ is the saturated mass density of the mixture [cf. (2)]. For bifurcation analysis it is more useful to consider the rate form of (22), which is given by

$$\mathrm{DIV}(\dot{\boldsymbol{P}})+\dot{\rho}_0\mathbf{g}=\mathbf{0}, \tag{23}$$

where

$$\dot{\rho}_0\equiv\frac{\mathrm{d}(J\rho)}{\mathrm{d}t}=J(\dot{\rho}^{\mathrm{s}}+\dot{\rho}^{\mathrm{f}})+\dot{J}(\rho^{\mathrm{s}}+\rho^{\mathrm{f}}). \tag{24}$$

Since $\dot{J}=J\mathrm{div}(\boldsymbol{v})$, we get

$$\begin{aligned}\dot{\rho}_0&=J[\dot{\rho}^{\mathrm{s}}+\rho^{\mathrm{s}}\mathrm{div}(\boldsymbol{v})]+J[\dot{\rho}^{\mathrm{f}}+\rho^{\mathrm{f}}\mathrm{div}(\boldsymbol{v})]\\&=-J\mathrm{div}(\boldsymbol{q})=-\mathrm{DIV}(\boldsymbol{Q})\end{aligned} \tag{25}$$

after using the mass balance equations (6) and (7). Hence, the Piola transform $\boldsymbol{Q}$ has the physical significance that its divergence with respect to the reference configuration is the negative of the time derivative (with respect to the solid motion) of the pull-back mass density $\rho_0$. Note that for a mixture of two or more constituents, $\dot{\rho}_0=0$ if there is no relative flow of the fluid relative to the solid matrix.

A critical aspect of balance of linear momentum for a mixture of two or more constituents lies in the decomposition of the total stress tensor. To this end we recall the following stress tensor decomposition emerging from continuum principles of thermodynamics in the absence of non-mechanical energy for a solid matrix whose voids are completely filled with fluid [7]:

$$\boldsymbol{\sigma}=\boldsymbol{\sigma}'-Bp_{\mathrm{f}}\mathbf{1}, \tag{26}$$

where $\boldsymbol{\sigma}$ is the total Cauchy stress tensor, $\boldsymbol{\sigma}'$ is a constitutive (or effective) Cauchy stress that is energy-conjugate to the rate of deformation of the solid matrix, and $\mathbf{1}$ is the second-order identity tensor (Kronecker delta). As a matter of sign convention, a positive normal stress implies tension in the present case. The stress quantity $\boldsymbol{\sigma}'$ in (26) is known as the Nur and Byerlee [29] effective stress, which reduces to the Terzaghi [34] effective stress when $B=1$.

Multiplying both sides of (26) by $J$ gives

$$\boldsymbol{\tau}=\boldsymbol{\tau}'-B\theta_{\mathrm{f}}\mathbf{1}, \tag{27}$$

where $\boldsymbol{\tau}=J\boldsymbol{\sigma}$ and $\boldsymbol{\tau}'=J\boldsymbol{\sigma}'$ are the symmetric total and effective Kirchhoff stress tensors, respectively. Contracting the right index of $\boldsymbol{\tau}$ by $\boldsymbol{F}^{-\mathrm{t}}$ gives

$$\boldsymbol{P}=\boldsymbol{P}'-B\theta_{\mathrm{f}}\boldsymbol{F}^{-\mathrm{t}}, \tag{28}$$

where $\boldsymbol{P}=\boldsymbol{\tau}\cdot\boldsymbol{F}^{-\mathrm{t}}$ and $\boldsymbol{P}'=\boldsymbol{\tau}'\cdot\boldsymbol{F}^{-\mathrm{t}}$. Taking the time derivative of (28) with respect to the solid motion gives

$$\dot{\boldsymbol{P}}=\dot{\boldsymbol{P}}'-B\dot{\theta}_{\mathrm{f}}\dot{\boldsymbol{F}}^{-\mathrm{t}}-B\dot{\theta}_{\mathrm{f}}\boldsymbol{F}^{-\mathrm{t}}-\dot{B}\theta_{\mathrm{f}}\boldsymbol{F}^{-\mathrm{t}}, \tag{29}$$

where $\dot{B}=-\dot{K}/K_{\mathrm{s}}$.

We now put these results together. For the solid body $\mathcal{B}$, let $\partial\mathcal{B}=\overline{\partial\mathcal{B}_t\cup\partial\mathcal{B}_u}$ and $\emptyset=\partial\mathcal{B}_t\cap\partial\mathcal{B}_u$; and where $\partial\mathcal{B}_t$ and $\partial\mathcal{B}_u$ are portions of the entire boundary where nominal traction rates and solid velocities are prescribed. Note that the same boundary $\partial\mathcal{B}$ was decomposed earlier into $\partial\mathcal{B}_\theta$ and $\partial\mathcal{B}_q$, which have no connection with $\partial\mathcal{B}_t$ and $\partial\mathcal{B}_u$.

For the momentum equation we denote the solution pair by $(\dot{\boldsymbol{P}},\boldsymbol{v})$, and to be admissible we must have

$$\mathrm{DIV}(\dot{\boldsymbol{P}})-\mathrm{DIV}(\boldsymbol{Q})\mathbf{g}=\mathbf{0} \qquad \text{in } \mathcal{B} \tag{30}$$

$$\boldsymbol{v} = \dot{\boldsymbol{u}}_0 \quad \text{on } \partial\mathcal{B}_u \tag{31}$$

$$\dot{\boldsymbol{P}} \cdot \boldsymbol{N} = \dot{\boldsymbol{t}}_0 \quad \text{on } \partial\mathcal{B}_t \tag{32}$$

where $\boldsymbol{N}$ is the unit outward normal vector to $\partial\mathcal{B}$, and $\boldsymbol{u}_0$ and $\boldsymbol{t}_0$ are prescribed boundary displacements and nominal tractions, respectively.

## 3 Local stability and uniqueness

Suppose we consider an alternative solution pair $(\dot{\boldsymbol{P}}^*, \boldsymbol{v}^*) \neq (\dot{\boldsymbol{P}}, \boldsymbol{v})$ that also satisfies the partial differential equation (30) and boundary conditions (31) and (32). We explore the existence of this alternative solution with the trivial identity

$$\begin{aligned}\int_{\mathcal{B}} \mathrm{DIV}[(\boldsymbol{v}^* - \boldsymbol{v}) \cdot (\dot{\boldsymbol{P}}^* - \dot{\boldsymbol{P}})]\mathrm{d}V \\ = \int_{\mathcal{B}} (\dot{\boldsymbol{F}}^* - \dot{\boldsymbol{F}}) : (\dot{\boldsymbol{P}}^* - \dot{\boldsymbol{P}})\mathrm{d}V \\ + \int_{\mathcal{B}} (\boldsymbol{v}^* - \boldsymbol{v}) \cdot [\mathrm{DIV}(\dot{\boldsymbol{P}}^*) - \mathrm{DIV}(\dot{\boldsymbol{P}})]\mathrm{d}V.\end{aligned} \tag{33}$$

In addition, we augment the integral equation above with balance of mass,

$$\begin{aligned}\int_{\mathcal{B}} \left[ \left( B - \frac{p^{\mathrm{f}}}{K_{\mathrm{f}}} \right) (\dot{J}^* - \dot{J}) + \frac{\phi^{\mathrm{f}}}{K_{\mathrm{f}}} (\dot{\theta}_{\mathrm{f}}^* - \dot{\theta}_{\mathrm{f}}) \right. \\ \left. + \frac{1}{\rho_{\mathrm{f}}} \mathrm{DIV}(\boldsymbol{Q}^* - \boldsymbol{Q}) \right] \mathrm{d}V = 0,\end{aligned} \tag{34}$$

in which $\dot{J}^*$ is kinematically linked with $\boldsymbol{v}^*$, and $(\dot{\theta}_{\mathrm{f}}^*, \boldsymbol{Q}^*)$ also constitutes an alternative solution pair that may be different from $(\dot{\theta}_{\mathrm{f}}, \boldsymbol{Q})$. By Gauss theorem the integral on the left-hand side of (33) is

$$\begin{aligned}\int_{\mathcal{B}} \mathrm{DIV}[(\boldsymbol{v}^* - \boldsymbol{v}) \cdot (\dot{\boldsymbol{P}}^* - \dot{\boldsymbol{P}})]\mathrm{d}V \\ = \int_{\partial\mathcal{B}} (\boldsymbol{v}^* - \boldsymbol{v}) \cdot (\dot{\boldsymbol{P}}^* - \dot{\boldsymbol{P}}) \cdot \boldsymbol{N}\, \mathrm{d}A = 0,\end{aligned} \tag{35}$$

since both solutions are required to satisfy the boundary conditions (31) and (32).

Now, we consider the condition $[\![\boldsymbol{Q}]\!] = \boldsymbol{Q}^* - \boldsymbol{Q} = \boldsymbol{0}$. This case is of interest since it suggests that the jump from one solution to the other occurs in the absence of fluid flow. This is not to say that $\boldsymbol{Q}$ itself is zero—drainage could still occur during deformation. By using the jump that occurs at bifurcation, we thus distinguish between local undrained deformation ($\boldsymbol{Q} = \boldsymbol{0}$) and local undrained bifurcation ($[\![\boldsymbol{Q}]\!] = \boldsymbol{0}$). For the latter case the second integral on the right-hand side of (33) is zero since both solutions are required to satisfy the momentum balance equation (30) for a fixed flow vector $\boldsymbol{Q}$. Thus, any pair of possible solutions must satisfy the condition

$$\int_{\mathcal{B}} (\dot{\boldsymbol{F}}^* - \dot{\boldsymbol{F}}) : (\dot{\boldsymbol{P}}^* - \dot{\boldsymbol{P}})\mathrm{d}V = 0, \tag{36}$$

subject to the constraint

$$\int_{\mathcal{B}} \left[ \left( B - \frac{p^{\mathrm{f}}}{K_{\mathrm{f}}} \right) (\dot{J}^* - \dot{J}) + \frac{\phi^{\mathrm{f}}}{K_{\mathrm{f}}} (\dot{\theta}_{\mathrm{f}}^* - \dot{\theta}_{\mathrm{f}}) \right] \mathrm{d}V = 0. \tag{37}$$

Uniqueness is guaranteed for every point and every pair of stresses and deformation gradients linked by the constitutive equation if

$$(\dot{\boldsymbol{F}}^* - \dot{\boldsymbol{F}}) : (\dot{\boldsymbol{P}}^* - \dot{\boldsymbol{P}}) > 0, \tag{38}$$

subject to the constraint

$$\left( B - \frac{p^{\mathrm{f}}}{K_{\mathrm{f}}} \right) (\dot{J}^* - \dot{J}) + \frac{\phi^{\mathrm{f}}}{K_{\mathrm{f}}} (\dot{\theta}_{\mathrm{f}}^* - \dot{\theta}_{\mathrm{f}}) = 0. \tag{39}$$

In this case the material is said to be incrementally stable. Note that this definition of stability does not depend on the flow boundary conditions—balance of mass is viewed only as a constraint on the mode shape on what is otherwise a classical solid mechanics stability problem.

Uniqueness is lost when the jump in the first Piola–Kirchhoff stress rate vanishes, i.e.

$$[\![\dot{\boldsymbol{P}}]\!] = \dot{\boldsymbol{P}}^* - \dot{\boldsymbol{P}} = \boldsymbol{0}. \tag{40}$$

This is a stronger condition than simply requiring that the inner product in (38) vanish by orthogonality. In an appendix at the end of this paper, we demonstrate that for incrementally linear materials the 'milder' orthogonality condition produces additional skew-symmetric terms that could violate the equilibrium condition. Hence, we shall choose the condition of stationary stress rate, (40), as our relevant criterion for loss of incremental stability.

The formulation simplifies considerably in the spatial description. Recall that $\boldsymbol{\tau} = \boldsymbol{P} \cdot \boldsymbol{F}^{\mathrm{t}}$; taking the time derivatives and evaluating the jumps in the rates we obtain

$$[\![\dot{\boldsymbol{\tau}}]\!] = \boldsymbol{P} \cdot [\![\dot{\boldsymbol{F}}^{\mathrm{t}}]\!] + [\![\dot{\boldsymbol{P}}]\!] \cdot \boldsymbol{F}^{\mathrm{t}}, \tag{41}$$

where

$$[\![\dot{\boldsymbol{F}}]\!] = [\![\boldsymbol{l}]\!] \cdot \boldsymbol{F}, \qquad [\![\boldsymbol{l}]\!] = \frac{\partial [\![\boldsymbol{v}]\!]}{\partial \boldsymbol{x}} = \frac{\partial (\boldsymbol{v}^* - \boldsymbol{v})}{\partial \boldsymbol{x}} = \boldsymbol{l} - \boldsymbol{l}^*, \tag{42}$$

and $[\![\boldsymbol{l}]\!]$ is the jump in the velocity gradient. Setting $[\![\dot{\boldsymbol{P}}]\!] = \boldsymbol{0}$ in (41) results in the equivalent condition for loss of local stability associated with a stationary stress rate

$$[\![\dot{\boldsymbol{\tau}}]\!] - (\boldsymbol{\tau} \ominus \boldsymbol{1}) : [\![\boldsymbol{l}]\!] = \boldsymbol{0}, \tag{43}$$

where $(\boldsymbol{\tau} \ominus \boldsymbol{1})_{ijkl} = \tau_{il}\delta_{jk}$, and $\delta_{jk}$ = Kronecker delta. The jump in the total Kirchhoff stress rate in this case may be obtained from (27) as

$$[\![\dot{\boldsymbol{\tau}}]\!] = [\![\dot{\boldsymbol{\tau}}']\!] - [\![\dot{B}]\!]\theta_{\mathrm{f}}\boldsymbol{1} - B[\![\dot{\theta}_{\mathrm{f}}]\!]\boldsymbol{1}, \quad [\![\dot{B}]\!] = -[\![\dot{K}]\!]/K_{\mathrm{s}}. \tag{44}$$

We now consider the following incremental constitutive equation

$$\dot{\boldsymbol{\tau}}' = \boldsymbol{\alpha} : \boldsymbol{l}, \qquad \dot{\boldsymbol{\tau}}'^{*} = \boldsymbol{\alpha} : \boldsymbol{l}^{*}, \tag{45}$$

where $\boldsymbol{\alpha}$ is a rank-four tensor with minor symmetry on its first two left indices but not on its last two right indices. We note two important points from the above relations: (a) the constitutive equation relates the Kirchhoff effective stress rate tensor $\dot{\boldsymbol{\tau}}'$ with the velocity gradient $\boldsymbol{l}$ as motivated by continuum principles of thermodynamics; and (b) the same tangent constitutive tensor $\boldsymbol{\alpha}$ is used irrespective of the direction of the velocity gradient. The latter point characterizes an incrementally linear material whose implication to elastoplasticity we shall elaborate in the next section. For completeness we shall also assume the following constitutive law for the bulk modulus $K$ of the solid matrix [cf. (12)]:

$$\dot{K} = C\phi^{\mathrm{s}}\dot{p}_{\mathrm{s}} = -CK\mathrm{div}(\boldsymbol{v}) = -CK\mathrm{tr}(\boldsymbol{l}), \tag{46}$$

where $C$ is a positive coefficient. This relation effectively yields a solid matrix bulk modulus that varies linearly with the solid pressure, a commonly observed feature of soil behavior.

Combining the above results yields the following condition for a stationary stress rate

$$\boldsymbol{\beta} : [\![\boldsymbol{l}]\!] - B\boldsymbol{1}[\![\dot{\theta}_{\mathrm{f}}]\!] = \boldsymbol{0}, \tag{47}$$

subject to the constraint

$$\left(B - \frac{p^{\mathrm{f}}}{K_{\mathrm{f}}}\right)\boldsymbol{1} : [\![\boldsymbol{l}]\!] + \frac{\phi^{\mathrm{f}}}{JK_{\mathrm{f}}}[\![\dot{\theta}_{\mathrm{f}}]\!] = 0, \tag{48}$$

where

$$\boldsymbol{\beta} := \boldsymbol{\alpha} - \boldsymbol{\tau} \ominus \boldsymbol{1} - C\theta_{\mathrm{f}}\frac{K}{K_{\mathrm{s}}}\boldsymbol{1} \otimes \boldsymbol{1}. \tag{49}$$

We can, of course, solve the above problem in many ways. For example, we can eliminate $[\![\dot{\theta}_{\mathrm{f}}]\!]$ from (48) and substitute into (47) to obtain the eigenvalue problem

$$\boldsymbol{\kappa} : [\![\boldsymbol{l}]\!] = \boldsymbol{0}, \tag{50}$$

where

$$\boldsymbol{\kappa} = \boldsymbol{\beta} + \frac{JBK_{\mathrm{f}}}{\phi^{\mathrm{f}}}\left(B - \frac{p^{\mathrm{f}}}{K_{\mathrm{f}}}\right)\boldsymbol{1} \otimes \boldsymbol{1} \tag{51}$$

is the undrained constitutive tensor. For a nontrivial solution $[\![\boldsymbol{l}]\!] \neq \boldsymbol{0}$ to exist we must have

$$\det(\boldsymbol{\kappa}) = 0. \tag{52}$$

The eigenmode (e-mode) $[\![\boldsymbol{l}]\!]$ of the singular tensor $\boldsymbol{\kappa}$ describes the 'shape' of the instantaneous jump.

## 4 Elastoplasticity and condition for liquefaction

For elastoplastic materials the component of the constitutive tensor $\boldsymbol{\alpha}$ in (45) depends on the loading direction $\dot{\boldsymbol{F}}$ and has two branches, one for elastic unloading and another for plastic loading. In principle we need to consider all possible loading/unloading scenarios to figure the most critical instability mode. In order to reduce the number of possible permutations we shall consider a so-called ''in-loading comparison solid'' [3, 18, 32] which guarantees loss of uniqueness according to definition (40).

### 4.1 Comparison solid

An e-mode defines a characteristic kinematical ''shape'' at bifurcation. It is important to know the correct sign of the e-mode since it determines if the volume will dilate or compact. To this end, we assume two possible velocity gradients $\boldsymbol{l}$ and $\boldsymbol{l}^{*}$ linked by the kinematical relation (42). Further, we assume a yield function of the form $F = F(\boldsymbol{\tau}, \kappa)$, where $\kappa$ is a plastic internal variable, and take $\boldsymbol{f} = \partial F/\partial\boldsymbol{\tau}$. The in-loading comparison solid postulates plastic loading everywhere, and so

$$\boldsymbol{f} : \boldsymbol{\alpha}^{\mathrm{e}} : \boldsymbol{l} > 0, \qquad \boldsymbol{f} : \boldsymbol{\alpha}^{\mathrm{e}} : \boldsymbol{l}^{*} > 0, \tag{53}$$

where $\boldsymbol{\alpha}^{\mathrm{e}}$ is the elastic component of the moduli tensor $\boldsymbol{\alpha}$. Since the two velocity gradients are linked by the equation $\boldsymbol{l}^{*} = \boldsymbol{l} + [\![\boldsymbol{l}]\!]$, it follows that

$$\boldsymbol{f} : \boldsymbol{\alpha}^{\mathrm{e}} : [\![\boldsymbol{l}]\!] > 0. \tag{54}$$

This last equation is our criterion for selecting the sign of the e-mode.

For the same in-loading comparison solid let $\boldsymbol{g} = \partial G/\partial \boldsymbol{\tau}$, where $G$ is the plastic potential function. As usual, the flow rule is associative if $\boldsymbol{g} = \boldsymbol{f}$. The tangent operator $\boldsymbol{\alpha}$ specializes to the form

$$\boldsymbol{\alpha}^{\mathrm{ep}} = \boldsymbol{\alpha}^{\mathrm{e}} - \frac{1}{\chi}\boldsymbol{\alpha}^{\mathrm{e}} : \boldsymbol{g} \otimes \boldsymbol{f} : \boldsymbol{\alpha}^{\mathrm{e}}, \tag{55}$$

where $\chi = \boldsymbol{f} : \boldsymbol{\alpha}^{\mathrm{e}} : \boldsymbol{g} + H > 0$, and where $H$ is the plastic modulus. The elastoplastic tensors $\boldsymbol{\beta}^{\mathrm{ep}}$ and $\boldsymbol{\kappa}^{\mathrm{ep}}$ may be constructed accordingly. For the in-loading comparison solid the condition for undrained bifurcation takes the form

$$\det(\boldsymbol{\kappa}^{\mathrm{ep}}) = 0. \tag{56}$$

Since the sign of the e-mode is known, we can determine whether the instantaneous volume change is implosive ($\mathrm{tr}[\![\boldsymbol{l}]\!] < 0$), explosive ($\mathrm{tr}[\![\boldsymbol{l}]\!] > 0$), or isochoric ($\mathrm{tr}[\![\boldsymbol{l}]\!] = 0$). Furthermore, (48) uniquely determines the sign of the pore pressure jump. Since $(B\text{–}p^{\mathrm{f}}/K_{\mathrm{f}}) > 0$ and $\phi^{\mathrm{f}}/(JK_{\mathrm{f}}) > 0$ in general, it follows that $\mathrm{tr}[\![\boldsymbol{l}]\!]$ and $[\![\dot{\theta}_{\mathrm{f}}]\!]$ have opposite signs.

### 4.2 Isotropic elastoplasticity

We consider in this section the case of isotropic plasticity to highlight the connection between the stability analysis presented in this paper and the onset of liquefaction instability in saturated granular soils. An important tool is the spectral decomposition of symmetric second-order tensors, and for the symmetric effective Kirchhoff stress tensor it takes the form

$$\boldsymbol{\tau}' = \sum_{A=1}^{3} \tau'_A \boldsymbol{m}^{(A)}, \qquad \boldsymbol{m}^{(A)} = \boldsymbol{n}^{(A)} \otimes \boldsymbol{n}^{(A)}, \tag{57}$$

where $\tau_A$ is a principal value with associated principal direction $\boldsymbol{n}^{(A)}$. The spectral directions satisfy the identity $\sum_{A=1}^{3} \boldsymbol{m}^{(A)} = 1$, so the total Kirchhoff stress tensor may be obtained from (27) as

$$\boldsymbol{\tau} = \sum_{A=1}^{3} \tau_A \boldsymbol{m}^{(A)}, \qquad \tau_A = \tau'_A - B\theta_{\mathrm{f}}. \tag{58}$$

The elastoplastic tangent tensor $\boldsymbol{\alpha}^{\mathrm{ep}}$ can also be decomposed spectrally,

$$\boldsymbol{\alpha}^{\mathrm{ep}} = \sum_{A=1}^{3}\sum_{B=1}^{3} \alpha_{AB} \boldsymbol{m}^{(A)} \otimes \boldsymbol{m}^{(A)} + \sum_{A=1}^{3}\sum_{B\neq A} \frac{\tau_B - \tau_A}{\lambda_B - \lambda_A} \Lambda^{(AB)}, \tag{59}$$

where

$$\Lambda^{(AB)} = \lambda_B \boldsymbol{m}^{(AB)} \otimes \boldsymbol{m}^{(AB)} + \lambda_A \boldsymbol{m}^{(AB)} \otimes \boldsymbol{m}^{(BA)}, \tag{60}$$

$\boldsymbol{m}^{(AB)} = \boldsymbol{n}^{(A)} \otimes \boldsymbol{n}^{(B)}$, $\alpha_{AB}$ is the $3 \times 3$ elastoplastic matrix in principal axes, and $\lambda_A$ is the elastic principal stretch.

The jump in the velocity gradient can also be written in spectral form. First, we recall the polar and spectral decompositions

$$\boldsymbol{F} = \boldsymbol{V} \cdot \boldsymbol{R}, \qquad \boldsymbol{V} = \sum_{A=1}^{3} \lambda_A \boldsymbol{m}^{(A)}, \tag{61}$$

where $\boldsymbol{R}$ is a proper orthogonal rotation tensor, $\lambda_A$ is a principal stretch, and $\boldsymbol{n}^{(A)}$ is a principal direction of the left stretch tensor $\boldsymbol{V}$ (which is coaxial with $\boldsymbol{\tau}$ by isotropy and in the absence of plastic spin). Taking the time derivative gives

$$\dot{\boldsymbol{F}} = \dot{\boldsymbol{V}} \cdot \boldsymbol{R} + \boldsymbol{V} \cdot \dot{\boldsymbol{R}} \tag{62}$$

where

$$\dot{\boldsymbol{V}} = \sum_{A=1}^{3} \dot{\lambda}_A \boldsymbol{m}^{(A)} + \sum_{A=1}^{3}\sum_{B\neq A} \omega_{AB}(\lambda_B - \lambda_A)\boldsymbol{m}^{(AB)}, \tag{63}$$

and $\omega_{AB}$ is the spin of the (Eulerian) principal axes of $\boldsymbol{V}$.

The velocity gradient can be expressed in the form

$$\boldsymbol{l} = \dot{\boldsymbol{F}} \cdot \boldsymbol{F}^{-1} = \dot{\boldsymbol{V}} \cdot \boldsymbol{V}^{-1} + \boldsymbol{V} \cdot \Omega \cdot \boldsymbol{V}^{-1}, \qquad \Omega = \dot{\boldsymbol{R}} \cdot \boldsymbol{R}^{\mathrm{t}}. \tag{64}$$

Using the spectral forms and taking the jumps, we get

$$[\![\boldsymbol{l}]\!] = \sum_{A=1}^{3} [\![\dot{\epsilon}_A]\!] \boldsymbol{m}^{(A)} + \sum_{A=1}^{3}\sum_{B\neq A} [\![\xi_{AB}]\!] \boldsymbol{m}^{(AB)}, \tag{65}$$

where

$$[\![\xi_{AB}]\!] = [\![\omega_{AB}]\!]\left(1 - \frac{\lambda_A}{\lambda_B}\right) + [\![w_{AB}]\!]\frac{\lambda_A}{\lambda_B} \tag{66}$$

is the jump in total spin, $w_{AB} = \Omega : \boldsymbol{m}^{(AB)}$, and $\epsilon_A = \ln \lambda_A$ is a principal logarithmic stretch. Note that $w_{AB}$ arises from the finite rotation of the stretch tensor $\boldsymbol{V}$ whereas $\omega_{AB}$ describes the spin of the principal axes of $\boldsymbol{V}$; the former vanishes in the infinitesimal theory whereas the latter generally does not. The particular e-mode of interest is characterized by $[\![\omega_{AB}]\!] = [\![w_{AB}]\!] = 0$, where the volume simply implodes at fixed $\boldsymbol{R}$ and at fixed spectral directions. In this case the jump in the velocity gradient takes the symmetric form

$$[\![\boldsymbol{l}]\!] = \sum_{A=1}^{3} [\![\dot{\epsilon}_A]\!] \boldsymbol{m}^{(A)}. \tag{67}$$

### 4.3 Condition for liquefaction

We now rewrite the condition for liquefaction instability. Let

$$\kappa_{AB} = \boldsymbol{m}^{(A)} : \boldsymbol{\kappa}^{\mathrm{ep}} : \boldsymbol{m}^{(B)} \tag{68}$$

For isotropic elastoplasticity the condition of stationary nominal stress rate may be written in principal directions as

$$\sum_{B=1}^{3} \kappa_{AB} [\![\dot{\epsilon}_B]\!] = 0. \tag{69}$$

For a non-trivial solution to exist we must have

$$\det(\kappa_{AB}) = 0. \tag{70}$$

This is the liquefaction condition in principal axes.

The e-mode is defined by the values of $[\![\dot{\epsilon}_B]\!]$ along with spectral representation (67), and its correct sign is determined from (54). Pore collapse is characterized by the condition

$$\mathrm{tr}[\![\boldsymbol{l}]\!] = \sum_{A=1}^{3} [\![\dot{\epsilon}_A]\!] < 0. \tag{71}$$

Note that the e-mode predicted above is diffuse in the sense that it does not entail the formation of a deformation band. The jump in the Kirchhoff pore pressure rate may be calculated accordingly as

$$[\![\dot{\theta}_{\mathrm{f}}]\!] = \frac{JK_{\mathrm{f}}}{\phi^{\mathrm{f}}} \left( B - \frac{p^{\mathrm{f}}}{K_{\mathrm{f}}} \right) \mathrm{tr}[\![\boldsymbol{l}]\!]. \tag{72}$$

Thus, we can calculate the accompanying jump in the pore pressure from the jump in $\mathrm{tr}(\boldsymbol{l})$.

Since $K_{\mathrm{f}}$ is typically large, $[\kappa_{AB}]$ may become ill-conditioned. In this case it may be best not to eliminate the pore pressure variable but instead use the full equations (47) and (48). Let

$$\beta_{AB} = \boldsymbol{m}^{(A)} : \boldsymbol{\beta}^{\mathrm{ep}} : \boldsymbol{m}^{(B)} \tag{73}$$

denote the drained elastoplastic tangent matrix in principal axes. The system of homogeneous equations can be written in the alternative full form

$$\underbrace{\begin{bmatrix} \beta_{11} & \beta_{12} & \beta_{13} & -B \\ \beta_{21} & \beta_{22} & \beta_{23} & -B \\ \beta_{31} & \beta_{32} & \beta_{33} & -B \\ -\overline{B} & -\overline{B} & -\overline{B} & -\phi^{\mathrm{f}}/(JK_{\mathrm{f}}) \end{bmatrix}}_{[\overline{\beta}]} \begin{Bmatrix} [\![\dot{\epsilon}_1]\!] \\ [\![\dot{\epsilon}_2]\!] \\ [\![\dot{\epsilon}_3]\!] \\ [\![\dot{\theta}_{\mathrm{f}}]\!] \end{Bmatrix} = \begin{Bmatrix} 0 \\ 0 \\ 0 \\ 0 \end{Bmatrix}, \tag{74}$$

where $\overline{B} = B - p^{\mathrm{f}}/K_{\mathrm{f}}$. For a nontrivial solution to exist we must have

$$\det[\overline{\boldsymbol{\beta}}] = 0. \tag{75}$$

equations (70) and (75) are, respectively, the penalty and Lagrange multipliers forms of the liquefaction condition in principal axes.

### 4.4 Infinitesimal theory, incompressibility, and axisymmetry

For soils the intrinsic bulk stiffnesses $K_{\mathrm{s}}$ and $K_{\mathrm{f}}$ are typically very high, relative to the stiffness of the solid matrix or skeleton, so the assumption of incompressible solid grains and fluids is not unreasonable.This yields $B = \overline{B} = 1$. Further, the infinitesimal theory is fully recovered by ignoring the initial stress term in the stiffness tensor, so the liquefaction condition in principal axes becomes

$$\begin{bmatrix} c_{11} & c_{12} & c_{13} & -1 \\ c_{21} & c_{22} & c_{23} & -1 \\ c_{31} & c_{32} & c_{33} & -1 \\ -1 & -1 & -1 & 0 \end{bmatrix} \begin{Bmatrix} [\![\dot{\epsilon}_1]\!] \\ [\![\dot{\epsilon}_2]\!] \\ [\![\dot{\epsilon}_3]\!] \\ [\![\dot{p}_{\mathrm{f}}]\!] \end{Bmatrix} = \begin{Bmatrix} 0 \\ 0 \\ 0 \\ 0 \end{Bmatrix}, \tag{76}$$

where $c_{IJ}$ are the small-strain constitutive moduli in principal axes and $\dot{\epsilon}_J$ are the principal strain rates. Note that the last row is simply the incompressibility constraint.

Axisymmetry, a geometric configuration typically utilized to describe a cylindrical soil sample loaded in triaxial testing, may be obtained from (76) by setting the first index to ''a'' (for axial) and the second and third indices to ''r'' (for radial). The third row becomes redundant, while the fourth row yields the incompressibility condition $[\![\dot{\epsilon}_{\mathrm{r}}]\!] = -[\![\dot{\epsilon}_{\mathrm{a}}]\!]/2$. After performing a static condensation, we obtain the reduced matrix form

$$\begin{bmatrix} (c_{\mathrm{aa}} - c_{\mathrm{ar}}) & -1 \\ (c_{\mathrm{ra}} - c_{\mathrm{rr}}) & -1 \end{bmatrix} \begin{Bmatrix} [\![\dot{\epsilon}_{\mathrm{a}}]\!] \\ [\![\dot{p}_{\mathrm{f}}]\!] \end{Bmatrix} = \begin{Bmatrix} 0 \\ 0 \end{Bmatrix}. \tag{77}$$

For a non-trivial solution to exist we must have

$$c_{\mathrm{aa}} + c_{\mathrm{rr}} - c_{\mathrm{ar}} - c_{\mathrm{ra}} = 0. \tag{78}$$

This is the liquefaction condition for a homogeneously deforming triaxial soil sample in the geometrically linear regime.

We now follow the classical framework of plasticity theory and assume yield and plastic potential functions $F$ and $G$, respectively. By isotropy we can express these

functions in terms of principal Cauchy effective stresses and define the gradients in principal axes as

$$f_A = \frac{\partial F}{\partial \sigma'_A}, \qquad g_B = \frac{\partial G}{\partial \sigma'_B}. \tag{79}$$

The elastoplastic constitutive matrix in principal axes has the standard form

$$c_{AB} = c^{\mathrm{e}}_{AB} - \frac{1}{\chi}\widetilde{g}_A \widetilde{f}_B \tag{80}$$

where

$$\widetilde{g}_A = \sum_{C=1}^{3} c^{\mathrm{e}}_{AC} g_C, \qquad \widetilde{f}_B = \sum_{C=1}^{3} c^{\mathrm{e}}_{BC} f_C,$$
$$\chi = \widetilde{\chi} + H > 0, \qquad \widetilde{\chi} = \sum_{A=1}^{3}\sum_{B=1}^{3} g_A c^{\mathrm{e}}_{AB} f_B > 0, \tag{81}$$

and $H$ is the plastic modulus.

Next we assume that the elastic moduli matrix in principal axes, $c^{\mathrm{e}}_{AB}$, is symmetric and positive definite, with components

$$c^{\mathrm{e}}_{AB} = \lambda I_{AB} + 2\mu\delta_{AB}, \tag{82}$$

where $I_{AB} = 1$ for all possible indices, $\lambda$ and $\mu$ are the elastic Lamé parameters, and $\delta_{AB}$ is the Kronecker delta. We are interested in finding a closed-form expression for the critical plastic modulus $H_{\mathrm{cr}}$, defined as the value of $H$ at which the determinant condition (78) is satisfied for the first time. Indeed, this expression is available in closed form, given by

$$H_{\mathrm{cr}} = \frac{1}{4\mu}(\widetilde{g}_{\mathrm{a}} - \widetilde{g}_{\mathrm{r}})(\widetilde{f}_{\mathrm{a}} - \widetilde{f}_{\mathrm{r}}) - \widetilde{\chi}. \tag{83}$$

An analog of $H_{\mathrm{cr}}$ for a shear band bifurcation has been derived by Rudnicki and Rice [33]. Suffice it to say that closed-form expressions for $H_{\mathrm{cr}}$ appear easier to derive for diffuse bifurcations than for localized bifurcations since we do not need to search for the critical band orientation with a diffuse mode.

## 5 Static liquefaction of loose Hostun RF sand

The undrained behavior of very loose Hostun RF sand has been the subject of much investigation [13, 14, 16, 25]. In this paper we shall use the triaxial laboratory test data reported by Doanh et al. [13] to demonstrate the implications of the proposed liquefaction condition.

### 5.1 Test data for isotropically consolidated samples

Doanh et al. [13] performed undrained triaxial compression and extension tests on isotropically and anisotropically consolidated samples of very loose Hostun RF sand. They used enlarged and lubricated end platens to produce relatively homogeneous deformations at large strains, and a triaxial testing machine with swivels at the top and bottom of the sample to eliminate moments from a possible eccentricity of the applied forces. In the following discussion we shall use their test data for the isotropically consolidated samples as a benchmark for the liquefaction instability analysis.

Figure 1 shows the stress paths on the $p$–$q$ plane for eight tests on isotropically consolidated samples, four for compression and four for extension, where $p = (\sigma_{\mathrm{a}}' + 2\sigma_{\mathrm{r}}')/3$ is the effective mean normal stress and $q = \sigma_{\mathrm{a}}' - \sigma_{\mathrm{r}}'$ is the deviator stress, and where $\sigma_{\mathrm{a}}'$ and $\sigma_{\mathrm{r}}'$ are the Cauchy axial and radial effective stresses, respectively (negative for compression, following the continuum mechanics convention). Initial effective consolidation pressures of 50, 100, 200 and 300 kPa are represented by curves 1–4, respectively. As expected, the peak deviator stress increases with initial confining pressure, and is greater for compression test than for extension test for the same initial confining stress, suggesting the influence of the third stress invariant. All stress paths intersected the $p$-axis at vertical slopes on the compression cap, suggesting that this cap is smooth at the transition from compression to extension.

Figure 2 shows the experimentally derived deviator stress versus axial strain curves for the compression and extension tests. Axial strains at peak deviator

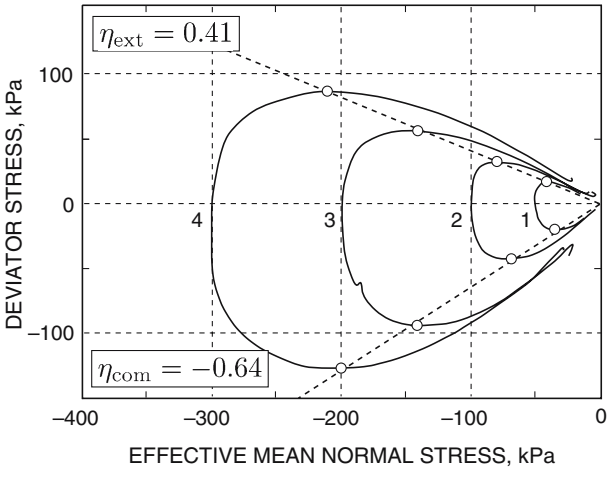


**Fig. 1** Stress paths for isotropically consolidated undrained triaxial compression and extension tests on Hostun RF sand. *Open circles* denote peak points. Reproduced from [13]

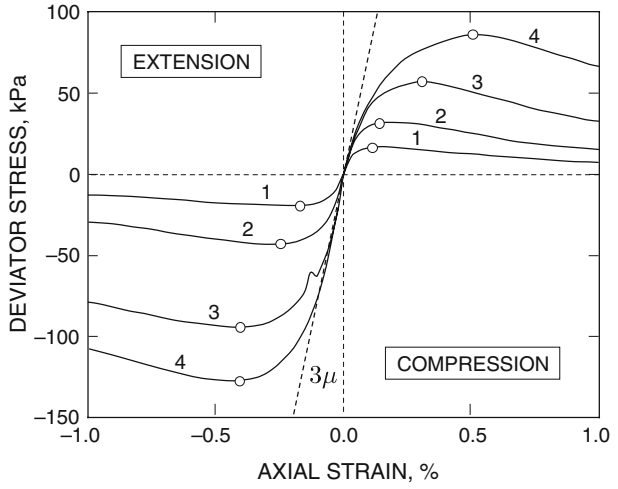


**Fig. 2** Deviator stress–axial strain curves for isotropically consolidated undrained triaxial compression and extension tests on Hostun RF sand. *Open circles* denote peak points. Reproduced from [13]

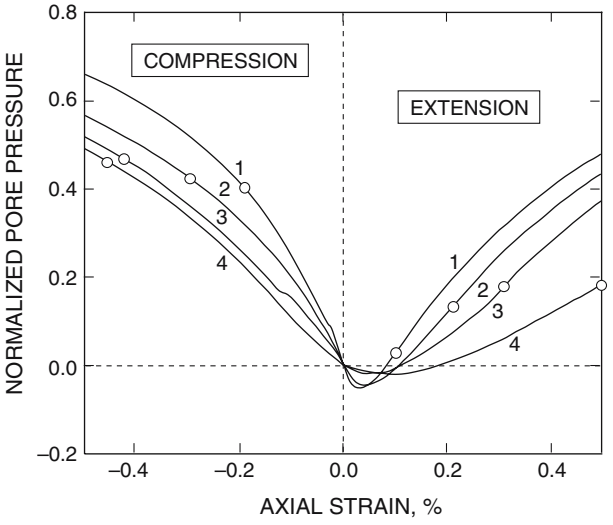


**Fig. 3** Pore pressure–axial strain curves for isotropically consolidated undrained triaxial compression and extension tests on Hostun RF sand. *Open circles* denote peak deviator stresses. Reproduced from [13]

stresses tend to increase with initial confining pressures at approximately 0.1–0.5%. These strains are quite small although testing was continued at post peak up until an axial strain of about 15%. For the given range of initial confining pressure the initial tangent modulus is nearly constant for all eight tests with an estimated value $3\mu = 75{,}000$ kPa, or $\mu = 25{,}000$ kPa. This modulus is significantly greater than the imposed stresses (on the order of a few hundred kPa), so assuming a constant elastic modulus and ignoring the initial stress terms in the stiffness matrix seem warranted for this range of pressures. Fig. 3 shows the experimentally derived pore pressure response curves normalized with respect to the initial confining pressures. All four extension tests exhibited an initially dilatant behavior (pore pressure decrease), followed by a compactive behavior (pore pressure increase), while all four compression tests exhibited a compactive behavior throughout.

Doanh et al. [13] also noted that none of the samples failed by deformation banding. Instead, liquefaction instability ensued following the peak stresses, characterized by a marked softening response accompanied by continued increase in pore pressure. 'Total liquefaction,' defined by the condition $p = q = 0$, was not achieved in any of the eight tests.

### 5.2 Analysis and discussions

Triaxial liquefaction tests are commonly simulated numerically with an axisymmetrically loaded element, the assumption being that the sample is deforming homogeneously. While this approach may be acceptable at low shear stresses, we have noted from previous works that the triggering of instabilities at high shear stresses is influenced to a great extent by the soil heterogeneity, such as the spatial density variation of the sample [1, 2, 8]. Such data are typically obtained from high-resolution imaging, but unfortunately they are not available for the present case study. Thus, we shall limit the discussion of this section to the ideal condition in which the soil specimen is deforming homogeneously in undrained triaxial extension and compression.

The stresses and pore pressures measured in the tests of Doanh et al. [13] were very low compared to the bulk moduli $K_s$ and $K_f$, so in the following we assume that the solid grains and fluids are incompressible. Undrained deformation then implies that the Jacobian determinant is $J = 1$, which means that the Cauchy and Kirchhoff stress tensors are the same. A typical analysis would involve 'fitting' yield and plastic potential functions $F$ and $G$ on test data and postulating a certain hardening/softening law. We shall not follow this traditional way of analysis but instead focus on describing the critical plastic modulus $H_{cr}$ and the associated e-mode at onset of liquefaction instability. These two aspects are critical for the eventual simulation of liquefaction phenomena as a boundary-value problem.

The premise of the analysis is as follows. Suppose the yield surface $F$ fits the experimental data exactly. Then we can construct normal vectors on the yield surface $F$ and measure the slope $m = m(\eta)$, where

$$m(\eta) = \frac{\partial F/\partial q}{\partial F/\partial p}, \tag{84}$$

and $\eta = q/p$ is the stress ratio given by slopes of the radial lines emanating from the origin of the $p$–$q$ plane. In Fig. 4 we sketch normal vectors to a yield surface that passes through the data points for the 300 kPa confining pressure test. The normalized gradients with respect to the principal effective stresses at the same stress point are given by

$$f_a = -\frac{1+3m}{\sqrt{3+27m^2/2}}, \qquad f_r = -\frac{1-3m/2}{\sqrt{3+27m^2/2}}, \tag{85}$$

where $(f_a^2 + 2f_r^2)^{1/2} = 1$. We see in Fig. 4 that on the compression cap, $m < 0$ during triaxial extension and $m > 0$ during triaxial compression. The slope $m$ also defines the gradient to the plastic potential function in the case of associative flow rule.

In general the flow rule for sand is not associative [20] except perhaps at the nose of the compression cap and near the critical state line. To accommodate a non-associative plastic flow we also define a slope

$$\widetilde{m}(\eta) = \frac{\partial G/\partial q}{\partial G/\partial p}, \tag{86}$$

where $G$ is the plastic potential function, see Fig. 5. The slope $\widetilde{m}$ is generally steeper than $m$, although, in general, the two have the same sign. Replacing $m$ with $\widetilde{m}$ in (85) thus gives the relevant expressions for $g_a$ and $g_r$. The critical plastic modulus can then be written in terms of $m$ and $\widetilde{m}$ as

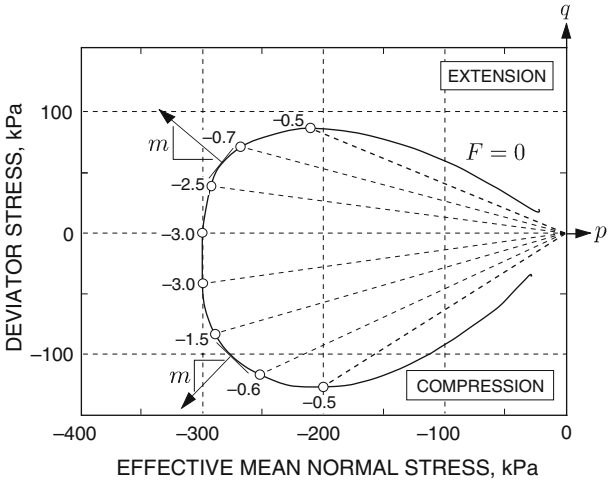


**Fig. 4** Definition of slope $m$, and variation of $H_{cr}/\mu$ with stress ratio $\eta = q/p$ assuming associated plastic flow. Critical hardening modulus is negative everywhere on the compression cap

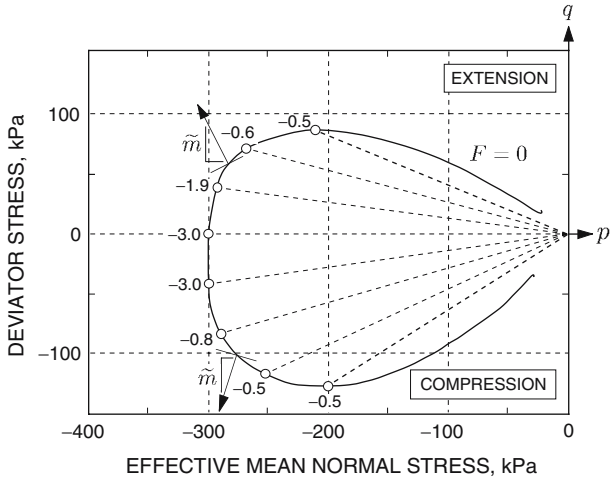


**Fig. 5** Definition of slope $\widetilde{m}$, and variation of $H_{cr}/\mu$ with stress ratio $\eta = q/p$ assuming non-associated plastic flow. Critical hardening modulus is negative everywhere on the compression cap

$$H_{cr}/\mu = -\frac{6+27m\widetilde{m}/4+9\lambda/\mu}{\sqrt{3+27m^2/2}\sqrt{3+27\widetilde{m}^2/2}}. \tag{87}$$

Since $\lambda$ and $\mu$ are nonnegative numbers, and since $m$ and $\widetilde{m}$ are assumed to have the same sign, then $H_{cr} < 0$ everywhere on the compression cap irrespective of the slopes. We caution, however, that this expression for $H_{cr}$ is not conservative in the presence of soil heterogeneity, since deformation then becomes three-dimensional (instead of axisymmetric), thus enhancing the onset of liquefaction instability. In other words, the *local* critical plastic modulus in a triaxially loaded soil specimen could in fact be greater than the expression given above.

We plot the calculated $H_{cr}/\mu$ at different stress points in Figs. 4 and 5, assuming a Poisson's ratio $\nu = 0.2$ for the soil skeleton (which gives $\lambda/\mu = 1/3$). Note that this parameter is a function solely of the slopes $m$ and $\widetilde{m}$. In Fig. 4 we assume an associative flow rule, whereas in Fig. 5 we assume a relation of the form $\widetilde{m} = m\exp(5|\eta|)$. The latter relation guarantees that the two slopes are the same at $\eta = 0$ and at $\eta = \eta_{peak}$, with $|\widetilde{m}| > |m|$ elsewhere to conform with experimental observations [20].

The following observations can be made from Figs. 4 and 5. First, shear stresses enhance the potential for liquefaction instability as can be observed from the fact that $H_{cr}$ increases with increasing $\eta$. This is commonly referred to as shear-induced liquefaction instability and is well known even from the early works of Castro [9, 10]. Shear-induced liquefaction instability is also linked to 'flow liquefaction' [19, 22, 35]. Second, a non-associative flow rule also enhances liquefaction

instability as can be seen from the fact that the plastic modulus is higher elsewhere between the nose and the peak point of the yield surface. What this means is that with a non-associative plastic flow there is a greater likelihood of liquefaction even below the peak stress if the actual plastic modulus matches the critical plastic modulus below the peak stress. This could have important implications to modeling liquefaction and other applications involving diffuse bifurcation as a boundary-value problem, see Chambon [11], Darve et al. [12], and Nova [28] for further discussions on diffuse instability.

### 5.3 E-mode at liquefaction

Finally, we use the simplified one-element representation of Hostun RF sand sample to obtain the e-mode at onset of liquefaction. To this end, suppose we have identified the critical condition at which $H = H_{\rm cr}$. At onset of liquefaction the in-loading comparison solid requires that [cf. (54)]

$$\sum_{A=1}^{3}\sum_{B=1}^{3} f_A \alpha^{\rm e}_{AB} [\![\dot{\epsilon}_B]\!] = -\frac{9m}{\sqrt{3+27m^2/2}}\mu [\![\dot{\epsilon}_{\rm a}]\!] > 0. \tag{88}$$

Thus, for triaxial compression testing where $m > 0$ we must have $[\![\dot{\epsilon}_{\rm a}]\!] < 0$, and for triaxial extension testing where $m < 0$ we must have $[\![\dot{\epsilon}_{\rm a}]\!] > 0$. The signs of these two jumps clearly check with the known kinematics of the two tests.

To determine the signs of the pore pressure jump we expand either row of the matrix equation (77) to yield

$$c[\![\dot{\epsilon}_{\rm a}]\!] - [\![\dot{p}_{\rm f}]\!] = 0, \tag{89}$$

where

$$\begin{aligned} c &= c_{\rm aa} - c_{\rm ar} = c_{ra} - c_{\rm rr} \\ &= -2\mu\frac{\widetilde{g}_{\rm a} + \widetilde{g}_{\rm r}}{\widetilde{g}_{\rm a} - \widetilde{g}_{\rm r}} = -\frac{12\lambda + (8+6\widetilde{m})\mu}{9\widetilde{m}}. \end{aligned} \tag{90}$$

For triaxial compression testing where $\widetilde{m} > 0$ we have $c < 0$, and since $[\![\dot{\epsilon}_{\rm a}]\!] < 0$ for this type of test we conclude that $[\![\dot{p}_{\rm f}]\!] > 0$. This is consistent with the known kinematics of liquefaction. On the other hand, for triaxial extension where $\widetilde{m} < 0$, we get $c > 0$ provided $\widetilde{m} > -2\lambda/\mu - 4/3$. In this case, $[\![\dot{p}_{\rm f}]\!] > 0$ since $[\![\dot{\epsilon}_{\rm a}]\!] > 0$. Note that $[\![\dot{p}_{\rm f}]\!]$ could switch sign and become negative if the slope $\widetilde{m}$ becomes too negatively large. Although not related to liquefaction, Fig. 3 does show that pore pressures in very loose saturated sands do indeed become negative in a more kinematically constrained stress state of triaxial extension.

## 6 Closure

We have used bifurcation theory to predict the onset of liquefaction instability and the associated e-modes in fully saturated granular soils. Liquefaction instability is equated with loss of uniqueness in the solution for the solid velocity and pore pressure rate under a locally undrained condition. The jumps in the strain rates define a nearly isochoric state of deformation and would otherwise be contractive if it were not for the presence of fluids. Note that this definition of liquefaction instability is not the same as 'total liquefaction' commonly associated with complete, or nearly complete, loss of contact forces between the solid grains. An advantage of the proposed formulation over the use of so-called flow liquefaction surface to predict liquefaction instability is that it captures the well-known kinematics of liquefaction in a general 3D setting, and is as robust as the now well-developed approach for predicting the onset of deformation bands. To conclude, we now have a unifying 3D theoretical framework that predicts whether the soil will form a deformation band (localized bifurcation), or will implode when it is dry (diffuse bifurcation), or will undergo liquefaction instability when it is saturated (diffuse bifurcation augmented with balance of mass).

Like the deformation band instability, liquefaction instability in soil samples should be analyzed as a boundary-value problem whenever possible. Soil heterogeneity plays a very critical role in the prediction of material instability. It has been shown to enhance shear band bifurcation, and there is no reason why it should not enhance the triggering of liquefaction instability. Soil liquefaction is a multiscale, multiphysics problem, originating at the pore scale but rapidly propagating to the specimen scale, so capture of the small scale effects is essential for an accurate prediction of the inception of this phenomenon. A viable approach for attacking the liquefaction problem in a truly multiscale fashion is to quantify the soil heterogeneity (e.g. spatial density variation) experimentally and use this information as input into detailed numerical meso-scale modeling efforts. Work in this area is currently in progress.

**Acknowledgments** Funding for this research was provided by the US National Science Foundation, Grant No. CMS-0201317, "Static and dynamic instability of liquefiable soils," under the directorship of the late Cliff Astill. This paper was written in his memory.

## 7 Appendix: Some notes on the stability conditions

Consider an incrementally linear material and take $\mathcal{A} = \partial \boldsymbol{P}/\partial \boldsymbol{F}$ so that $\dot{\boldsymbol{P}} = \mathcal{A} : \dot{\boldsymbol{F}}$ and $\dot{\boldsymbol{P}}^* = \mathcal{A} : \dot{\boldsymbol{F}}^*$ (i.e.

the same tangent operator is used for the two alternative solutions). We can write $\mathcal{A}$ as the sum of a symmetric part $\mathcal{A}^{\text{sym}}$ and a skew-symmetric part $\mathcal{A}^{\text{skw}}$. Loss of incremental stability occurs when

$$[\![\dot{\boldsymbol{F}}]\!] : [\![\dot{\boldsymbol{P}}]\!] = [\![\dot{\boldsymbol{F}}]\!] : \mathcal{A} : [\![\dot{\boldsymbol{F}}]\!] = [\![\dot{\boldsymbol{F}}]\!] : \mathcal{A}^{\text{sym}} : [\![\dot{\boldsymbol{F}}]\!] = 0. \quad (91)$$

Only the symmetric part survives since a skew-symmetric matrix automatically yields an orthogonal metric. Thus, loss of incremental stability occurs when

$$\det(\mathcal{A}^{\text{sym}}) = 0. \quad (92)$$

The jump $[\![\dot{\boldsymbol{F}}]\!]$ can be obtained as the e-vector (or e-tensor) of $\mathcal{A}^{\text{sym}}$ via the homogeneous equation

$$\mathcal{A}^{\text{sym}} : [\![\dot{\boldsymbol{F}}]\!] = \boldsymbol{0}. \quad (93)$$

In this case the jump in the stress rate is not zero but is equal to

$$[\![\dot{\boldsymbol{P}}]\!] = (\mathcal{A}^{\text{sym}} + \mathcal{A}^{\text{skw}}) : [\![\dot{\boldsymbol{F}}]\!] = \mathcal{A}^{\text{skw}} : [\![\dot{\boldsymbol{F}}]\!]. \quad (94)$$

Now, assume that $(\dot{\boldsymbol{P}}, \boldsymbol{v})$ satisfies (30). To see if the alternative solution $(\dot{\boldsymbol{P}}^*, \boldsymbol{v}^*)$ also satisfies this same equation, we write

$$\text{DIV}(\dot{\boldsymbol{P}}^*) - \text{DIV}(\boldsymbol{Q}^*)\mathbf{g} = \text{DIV}(\mathcal{A}^{\text{skw}} : [\![\dot{\boldsymbol{F}}]\!]) \neq \boldsymbol{0}. \quad (95)$$

Hence, the alternative solution does not satisfy the equilibrium condition when the loss of incremental stability is defined in the sense of (92) (unless $\mathcal{A}$ is symmetric).

To illustrate the deformation banding analog, we assume that the kinematical jump has the form $[\![\dot{\boldsymbol{F}}]\!] = \varphi \boldsymbol{m} \otimes \boldsymbol{N}$, where $\boldsymbol{m}$ and $\boldsymbol{N}$ are Cartesian vectors. Then

$$[\![\dot{\boldsymbol{F}}]\!] : [\![\dot{\boldsymbol{P}}]\!] = \varphi^2 \boldsymbol{m} \cdot \boldsymbol{A} \cdot \boldsymbol{m} = \varphi^2 \boldsymbol{m} \cdot \boldsymbol{A}^{\text{sym}} \cdot \boldsymbol{m} = 0, \quad (96)$$

where $\boldsymbol{A} = \boldsymbol{A}^{\text{sym}} + \boldsymbol{A}^{\text{skw}}$ is the acoustic tensor. Loss of strong ellipticity occurs when

$$\det(\boldsymbol{A}^{\text{sym}}) = 0. \quad (97)$$

The e-vector $\boldsymbol{m}$ may be obtained from the homogeneous equation

$$\boldsymbol{A}^{\text{sym}} \cdot \boldsymbol{m} = \boldsymbol{0}. \quad (98)$$

In this case the jump in the nominal traction rate vector is not zero but is equal to

$$[\![\dot{\boldsymbol{t}}]\!] = [\![\dot{\boldsymbol{P}}]\!] \cdot \boldsymbol{N} = \varphi \boldsymbol{A} \cdot \boldsymbol{m} = \varphi \boldsymbol{A}^{\text{skw}} \cdot \boldsymbol{m}, \quad (99)$$

for $\boldsymbol{A}^{\text{skw}} \neq \boldsymbol{0}$. We see that equilibrium is preserved only by ensuring that the stress and traction rates are stationary.

## References


1. Andrade JE, Borja RI (2006) Modeling deformation banding in dense and loose fluid-saturated sands. Finite Elem Anal Des. In review
2. Andrade JE, Borja RI (2006) Capturing strain localization in dense sands with random density. Int J Num Meths Eng 67:1531–1564
3. Bigoni D (1999) Bifurcation and instability of non-associative elastoplastic solids. In: Petryk H (Coordinator) CISM Lecture notes on the course: Material instabilities in elastic and plastic solids, Udine, September
4. de Boer (2000) Theory of porous media, Highlights in the historical development and current state. Springer, Berlin Heidelberg, New York
5. Borja RI (2004) Cam clay plasticity, Part V: A mathematical framework for three-phase deformation and strain localization analyses of partially saturated porous media. Comput Methods Appl Mech Eng 193:5301–5338
6. Borja RI (2006) Conditions for instabilities in collapsible solids including volume implosion and compaction banding. Acta Geotechnica 1:107–122
7. Borja RI (2006) On the mechanical energy and effective stress in saturated and unsaturated porous continua. Int J Solids Struct 43:1764–1786
8. Borja RI, Andrade JE (2006) Critical state plasticity. Part VI: meso-scale finite element simulation of strain localization in discrete granular materials. Comput Methods Appl Mech Eng 195:5115–5140
9. Castro G (1969) Liquefaction of sands. Harvard soil mechanics series 87, Harvard University, Cambridge
10. Castro G (1975) Liquefaction and cyclic mobility of sands. J Geotech Eng Div ASCE 101:551–569
11. Chambon R (2005) Some theoretical results about second order work, uniqueness, existence and controllability independent of the constitutive equation. J Eng Math 52:53–61
12. Darve F, Servant G, Laouafa F, Khoa HDV (2004) Failure in geomaterials: continuous and discrete analyses. Comput Methods Appl Mech Eng 193:3057–3085
13. Doanh T, Ibraim E, Matiotti R (1997) Undrained instability of very loose Hostun sand in triaxial compression and extension. Part 1: experimental observations. Mech Cohes-Frict Mat 2:47–70
14. Doanh T, Ibraim E, Dubujet Ph, Matiotti R, Herle I (1999) Static liquefaction of very loose Hostun RF sand: Experiments and modelling. In: Lade PV, Yamamuro JA (eds) Physics and mechanics of soil liquefaction. Balkema, Rotterdam, pp 17–28
15. Dobry R, Ng T (1992) Discrete modelling of stress-strain behavior of granular media at small and large strains. Eng Comput 9:129–143
16. Dubujet Ph, Doanh T (1997) Undrained instability of very loose Hostun sand in triaxial compression and extension. Part 2: theoretical analysis using an elastoplasticity model. Mech Cohes–Frict Mat 2:71–92
17. El Shamy U, Zeghal M (2005) Coupled continuum-discrete model for saturated granular soils. J Eng Mech ASCE 131:413–426

18. Hill R (1958) A general theory of uniqueness and stability in elastic-plastic solids. J Mech Phys Solids 6:236–249
19. Ishihara K (1993) Liquefaction and flow failure during earthquakes. Géotechnique 43:351–415
20. Kim MK, Lade PV (1988) Single hardening constitutive model for frictional materials I. Plastic potential function. Comput Geotech 5:307–324
21. Kramer SL (1996) Geotechnical earthquake engineering. Prentice-Hall, New Jersey
22. Kramer SL, Seed HB (1988) Initiation of soil liquefaction under static loading conditions. J Geotech Eng 114:412–430
23. Lade PV (1992) Static instability and liquefaction of loose fine sandy slopes. J Geotech Eng ASCE 118:51–71
24. Lade PV (1999) Instability of granular materials. In: Lade PV, Yamamuro JA (eds) Physics and mechanics of soil liquefaction. Balkema, Rotterdam, pp 3–16
25. Lancelot L, Shahrour I, Al Mahmoud M (2004) Instability and static liquefaction on proportional strain paths for sand at low stresses. J Eng Mech 130:1365–1372
26. Li C, Borja RI, Regueiro RA (2004) Dynamics of porous media at finite strain. Comput Methods Appl Mech Eng 193:3837–3870
27. Malvern LE (1969) Introduction to the mechanics of a continuous medium. Prentice-Hall, New Jersey
28. Nova R (1994) Controllability of the incremental response of soil specimens subjected to arbitrary loading programmes. J Mech Behav Mater 5:221–243
29. Nur A, Byerlee JD (1971) An exact effective stress law for elastic deformation of rock with fluids. J Geophys Res 77:890–990
30. Ogden RW (1984) Non-linear elastic deformations. Ellis Horwood, Chichester
31. Poulos SJ (1981) The steady state of deformation. J Geotech Eng Div ASCE 107:553–562
32. Raniecki B, Bruhns OT (1981) Bounds to bifurcation stresses in solids with non-associated plastic flow at finite strain. J Mech Phys Solids 29:153–172
33. Rudnicki JW, Rice JR (1975) Conditions for the localization of deformation in pressure-sensitive dilatant materials. J Mech Phys Solids 23:371–394
34. Terzaghi K (1943) Theoretical soil mechanics. Wiley, New York
35. Vaid YP, Chern JC (1985) Cyclic and monotonic undrained response of saturated sands. In: Khosla V (ed) Advances in the art of testing soils under cyclic conditions. ASCE, New York, pp 120–147
36. Vaid YP, Thomas J (1995) Liquefaction and post-liquefaction behavior of sand. J Geotech Eng ASCE 121:163–173
37. Vaid YP, Chung EKF, Kuerbis RH (1990) Stress path and steady state. Can Geotech J 27:1–7
38. Yamamuro JA, Lade PV (1998) Static liquefaction of very loose sands. Can Geotech J 34:905–917
39. Zeghal M, El Shamy U (2005) Micro-mechanical modeling of site liquefaction and remediation through cementation. GSP 133 earthquake engineering and soil dynamics, ASCE, p 11